A route for a strong increase of critical current in nanostrained iron-based superconductors

Toshinori Ozaki[1,2], Lijun Wu[1], Cheng Zhang[1], Jan Jaroszynski[3], Weidong Si[1], Juan Zhou[1], Yimei Zhu[1] & Qiang Li[1]

The critical temperature T_c and the critical current density J_c determine the limits to large-scale superconductor applications. Superconductivity emerges at T_c. The practical current-carrying capability, measured by J_c, is the ability of defects in superconductors to pin the magnetic vortices, and that may reduce T_c. Simultaneous increase of T_c and J_c in superconductors is desirable but very difficult to realize. Here we demonstrate a route to raise both T_c and J_c together in iron-based superconductors. By using low-energy proton irradiation, we create cascade defects in $FeSe_{0.5}Te_{0.5}$ films. T_c is enhanced due to the nanoscale compressive strain and proximity effect, whereas J_c is doubled under zero field at 4.2 K through strong vortex pinning by the cascade defects and surrounding nanoscale strain. At 12 K and above 15 T, one order of magnitude of J_c enhancement is achieved in both parallel and perpendicular magnetic fields to the film surface.

[1] Condensed Matter Physics and Materials Science Department, Brookhaven National Laboratory, Upton, New York 11973, USA. [2] Department of Nanotechnology for Sustainable Energy, Kwansei Gakuin University, 2-1 Gakuen, Sanda, Hyogo 669-1337, Japan. [3] National High Magnetic Field Laboratory, Florida State University, 1800 E. Paul Dirac Drive, Tallahassee, Florida 32310, USA. Correspondence and requests for materials should be addressed to T.O. (email: tozaki@kwansei.ac.jp) or to Q.L. (email: qiangli@bnl.gov).

Superconductor's lossless current flow enables the design of highly dense and compact equipment, and hence offers powerful opportunities for increasing the capacity and the efficiency of power grids[1,2]. Superconducting coils use magnetic fields to store energy with near zero energy loss and can power drive rotary machines. Three properties of superconductors important for energy applications are superconducting transition temperature (also known as critical temperature) T_c, upper critical field, and electrical current-carrying capacity. They arise from different aspects of the superconducting states. T_c is directly related to the mechanism of superconductivity. The superconducting state emerges at T_c from interactions between electrons that form the Cooper pairs. The upper critical field, H_{c2}, is the highest magnetic field at which superconductivity is finally suppressed. In contrast to T_c and H_{c2}, the current-carrying capacity, measured by the practical critical current density J_c, is governed by the vortex pinning strength, which is determined by the ability of defects in superconducting materials to pin the vortices carrying magnetic flux. Defects create local regions with depressed pairing potential, which can pin the vortices. By doing so, unfortunately, defects tend to preclude the Cooper pair formation and hence drive down the T_c of cuprates and iron-based superconductors with short coherence lengths. It is a very difficult and challenging task to raise T_c and J_c simultaneously by means of introducing defects in the same cuprates and iron-based superconducting materials. Tremendous efforts have been made so far to optimize the defects landscape, to enhance J_c, while keeping the degradation of T_c to a minimum in cuprates and iron-based superconductors. Indeed, great improvements in J_c have been obtained in cuprate and in iron-based superconducting films as well, by introducing artificially designed defects such as precipitate and columnar defects, but at the cost of T_c degradation[3–10].

Iron-based superconductors[11] have attracted much attention in potential high-field applications due to their relatively high T_c, high H_{c2}, and small anisotropy γ[12,13]. Recent reports show that high-quality epitaxial films have been grown on single crystal substrates, mostly used for exploring the fundamental properties of iron-based superconductors[8–10,14–18]. We have reported very high-J_c FeSe$_{0.5}$Te$_{0.5}$ (FST) films with CeO$_2$ buffer layer on single crystals and a metal substrate of coated conductors[16]. We found that further J_c improvement by controlled growth of pinning defects, in the iron-based superconducting films we processed, is becoming increasingly difficult. This motivated us to look for alternative routes. Ion irradiation is a well-established method for artificially introducing various defects into superconducting materials in a fairly predictable and controllable manner by choosing appropriate ion species and energy[3,19–22]. Transmission electron microscopy (TEM) cross-sectional images along the ion traces in 230 MeV Au-irradiated Bi$_2$Sr$_2$CaCu$_2$O$_x$ single crystals showed several types of morphology of defects from parallel columnar defects to disordered cascade defects, as the ion energy is decreased in the crystals[22]. It is also well known that light ion irradiations produce smaller damaged volume fractions in the target materials than heavy ion irradiation and requires a much higher dosage to produce enough defects for flux pinning because of the significantly large ionization loss. These defects produced by ion irradiation would account for the depression of T_c in YBa$_2$Cu$_3$O$_y$ (YBCO), which is proportional to the average number of defects[23]. Recently, a low-energy ion irradiation has been revisited and suggested as a practically feasible approach to improve flux pinning in YBCO[24–26]. In single crystals of iron-based superconductors, it has been found that ion irradiations, as a whole, improve J_c and its J_c enhancements persist up to much higher fluencies than in cuprate superconductors, although T_c is suppressed with increasing irradiation doses[27–29]. In contrast, the irradiated iron-based superconducting films have not shown as positive effects as found in single crystals[30,31]. It is clear that the key to the enhancement of J_c in superconductors is in the design of defect landscape that must be tailored to a superconductors' chemistry, crystal structure, and materials' geometric aspect.

Here we show a strategy on nanostructure control in iron-chalcogenide superconducting FST films with low-energy proton irradiation. Through extensive TEM characterization, we found nanoscale strain modulations in FST films irradiated with 1×10^{15} p cm^{-2} dose of 190 keV proton. Enhanced T_c^{zero} from 18.0 to 18.5 K is observed in the irradiated films due to the nanoscale compressive strain and proximity effect. The low-energy proton irradiation also yields self-field J_c enhancement from 0.9 MA cm^{-2} up to 1.4 MA cm^{-2} at 4.2 K. The cascade defects and nanoscale strain produced by low-energy proton irradiation are found to provide strong vortex pinning, resulting in remarkable enhancements of J_c at both zero field and high magnetic field in all temperatures, and high maximum pinning force $F_{p,max}$ of $\sim$120 GN m^{-3} for $H//ab$ at 27 T and 4.2 K.

Results

Transition temperature and microstructural analysis. Figure 1a,b show the temperature dependence of the normalized resistivity up to 9 T with $H//c$ for the FST film before and after 190 keV proton irradiation at 1×10^{15} p cm^{-2} fluence, respectively. We determine the T_c^{zero} and the irreversibility field (H_{irr}) using $0.01\rho_n$ criteria and H_{c2} using $0.9\ \rho_n$ criteria with $\rho_n = \rho(20 K)$. As previously reported[16], the CeO$_2$-buffered FST film (pristine film) exhibits enhanced $T_c^{zero} = 18.0$ K, which is $\sim$30% higher than that found in
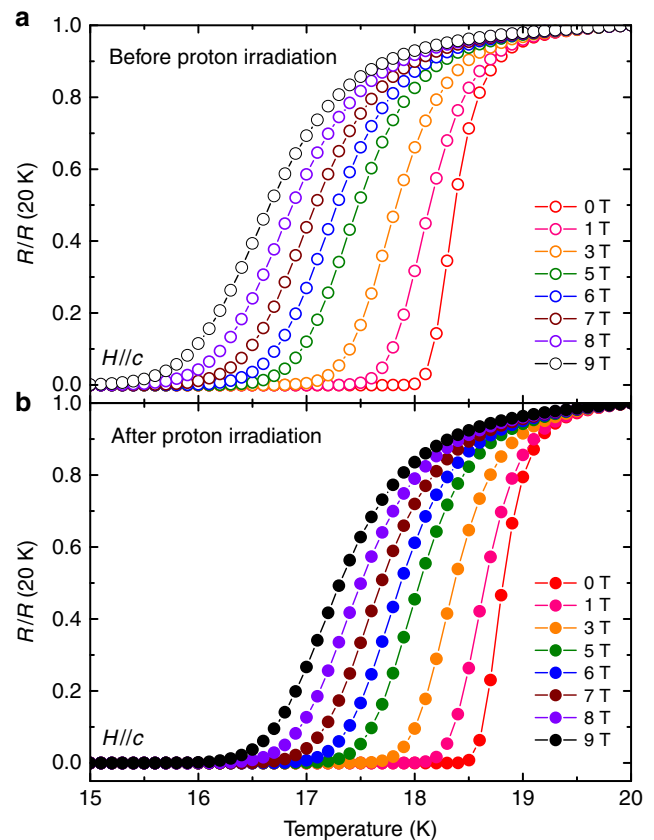
Figure 1 | Temperature dependence of normalized resistivity. $\rho(T)/\rho(20 K)$ at 0–9 T//c for the FST film before (**a**) and after (**b**) 190 keV proton irradiation with 1×10^{15} p cm^{-2} dose.

the bulk materials[32]. Strikingly, we found that the irradiated FST film does not show any T_c degradation, rather an increase of T_c by ~ 0.5 K. The enhancement of T_c by irradiations, with either light ion or heavy ion, was not known in iron-based superconductors previously[27–31].

In iron-chalcogenide superconductors, there have been many reports on enhancement of T_c for bulk materials[33–37], wires[38] and films[16,39–44]. Possible explanations can be grouped into three categories so far: (1) an interface effect, (2) an elimination of the influence of excess Fe at the interstitial sites of the Te/Se(S) layer and (3) a strain effect.

The first group is based on the observation of monolayer FeSe films on SrTiO₃ substrate[39,40]. The enhanced superconductivity is generally believed to be the result of the interface between two very different materials and not relevant to our FST film of ~ 100 nm thick.

The second group is based on the post-annealing effect[35–37]. This could be attributed to a reduction of excess Fe, which creates magnetic moments and causes pair breaking[45]. The reasonable concern could be raised that the enhancement of T_c in the proton-irradiated FST films is due to the suppression of the influence of excess Fe. To address this concern, we performed extensive high-resolution TEM (HRTEM) and scanning TEM (STEM) with high-angle annular dark field detector (HAADF) characterization. Figure 2a displays representative STEM–HAADF image of the pristine FST film. The FST film is epitaxially grown on the CeO₂ buffer layer. STEM–HAADF image also reveals the very sharp FST-CeO₂ interface without the chemical reaction layer reported in FST/CaF₂ interface[42]. What is more remarkable here is that excess Fe, which is supposed to occupy the interstitial site in many iron-chalcogenide bulk samples, is not present in the FST film. Note: the presence of excess Fe in the interstitial sites is one of the major issues in iron chalcogenide superconductor, which lowers H_{c2}. The absence of excess Fe in our FST films deposited by pulsed laser deposition method is consistent with the observation that these FST films retain excellent performance at high field[15,16,46]. This is of great advantage for high-field applications.

The third group is related to the strain effect on T_c (refs 33,34,38), especially in iron-chalcogenide superconducting films[16,41–44]. Figure 2b shows a cross-sectional HRTEM image of the FST film irradiated with 190 keV proton. We observed splayed cascade defects produced by proton irradiation over the entire film. An enlarged view of a typical defect is displayed in the inset. The stopping range of ions in matter model[47] predicts that with increasing depth in Al foil covered on the FST film (Supplementary Fig. 1), the angle distribution of the proton broadens, producing an angular splay for the proton. Previously, disordered spherical cascade defects were found to exist in the low-energy region of the Bi₂Sr₂CaCu₂Oₓ crystals[22]. Given that nuclear scattering events produce angular deviations from the original incident angle as the incident ions proceed through a target material, it is not surprising that light mass proton with a low energy of 190 keV easily tilted away from the original incident angle (0°) and create the disordered cascade defects.

According to Anderson's theorem[48], the T_c and the superconducting density of states in conventional s-wave superconductors are not affected by the non-magnetic impurity created by proton irradiation, whereas non-magnetic impurities can act as strong scattering centres and suppress T_c by pair breaking in d-wave[49] or $s\pm$ wave[50] superconductors. In striking contrast, here we observed enhanced T_c in the FST films after proton irradiation. Now we propose another mechanism to explain the enhancement of T_c by proton irradiation. We note that besides the clearly visible cascade, there is also a curvature of the lattice fringe inwardly directed, which produces strain field
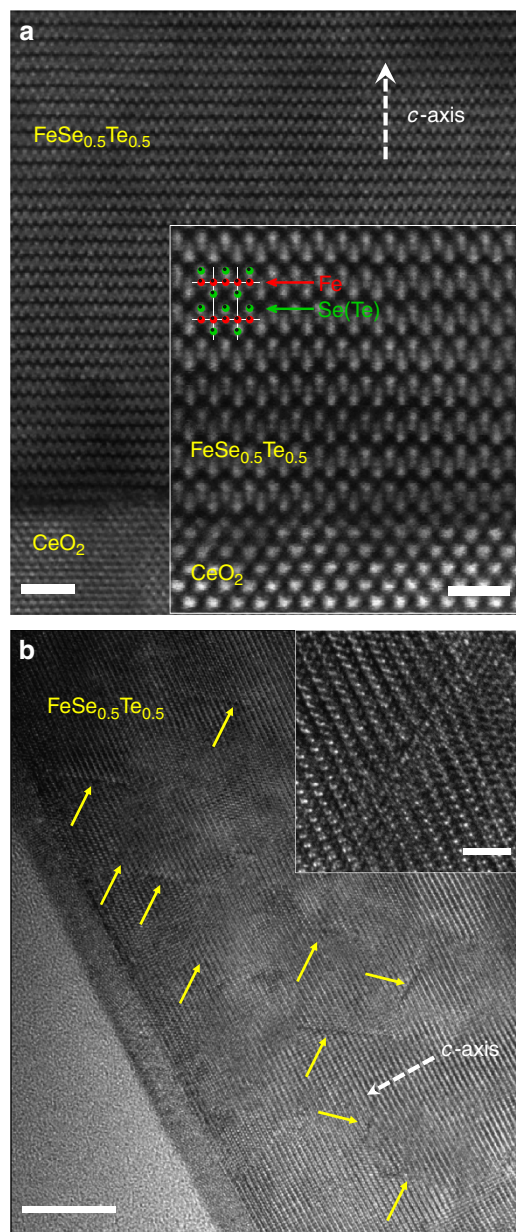
Figure 2 | Microstructure of FST films. (**a**) STEM-HAADF images of the representative FST film on the CeO₂ buffer layer. Scale bar, 2 nm. Inset: high-resolution image at the interface between CeO₂ and FST. Scale bar, 1 nm. (**b**) HRTEM image of FST film irradiated with 190 keV proton. Scale bar, 10 nm. Inset: high-resolution image of splayed cascade defect and strain field produced by 190 keV proton irradiation. Scale bar, 2 nm.

around the cascade defect. Similar strain fields created by low-energy proton and neutron irradiation were observed in YBCO single crystals from a previous TEM study[51,52]. Although the size of the cascade defects is about $1 \sim 2$ nm in diameter and ~ 10 nm wide, the strain fields are expected to extend far out to the cascade defect, especially in the radial direction and, as a result, can cause the local lattice distortion.

Origin of enhanced T_c and nanoscale lattice strain. To see the cascade defect induced local lattice distortion, we Fourier transform two circled areas I and II in Fig. 3a, to get the diffractogram of the area of interest, as shown in the inset I and II. Intensity
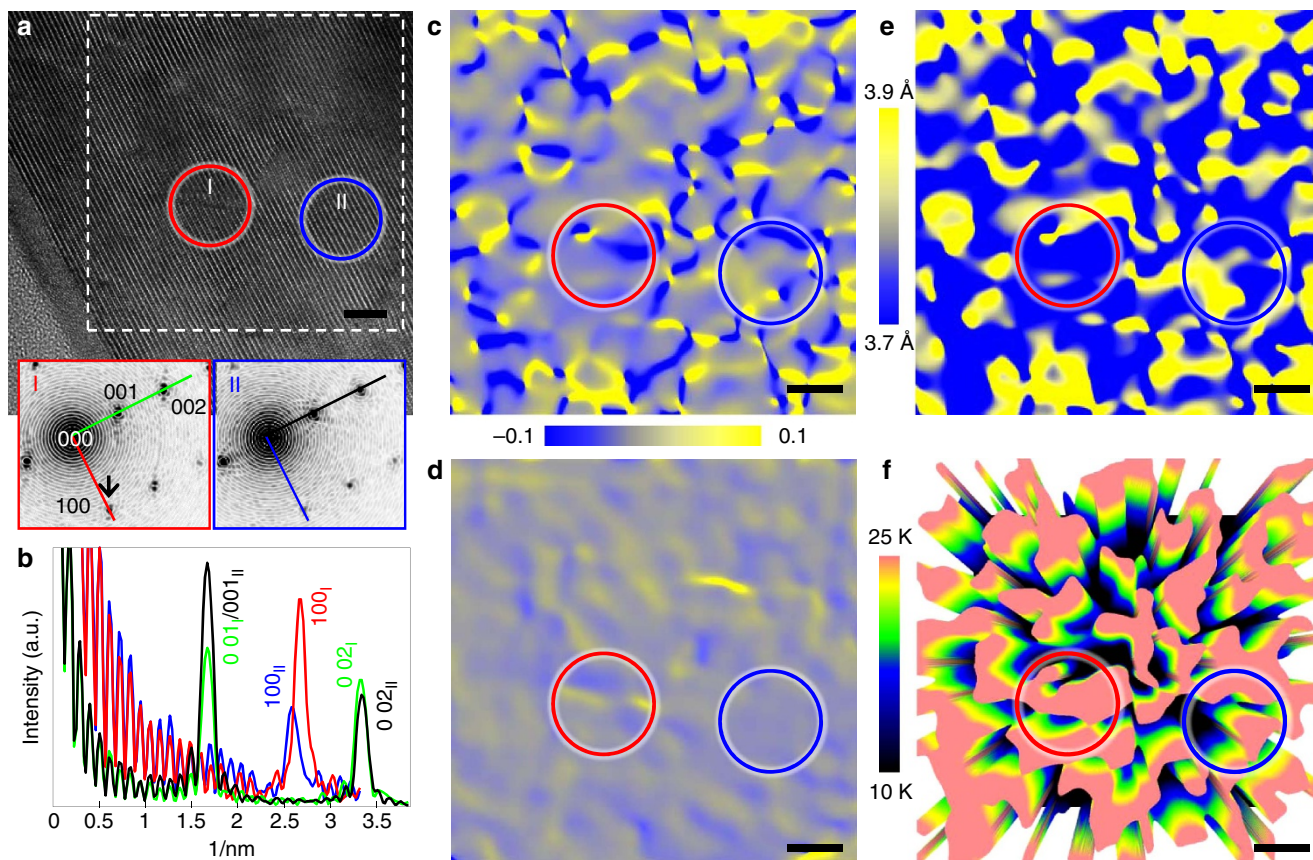
Figure 3 | Strain analysis in a 190 keV proton irradiated FST film. (**a**) HRTEM image. The inset I and II are the diffractogram from the circled area I (red) and II (blue), respectively. (**b**) Intensity line profiles of 001/002 (green and black) and 100 (red and blue) spots from the scan lines shown in the inset I and II of **a**. (**c,d**) Strain maps of in-plane ε_{xx} (**c**) and out-of-plane ε_{zz} (**d**) calculated by geometrical phase analysis (GPA)[53–55] from the square area outlined by dash line in **a**. The colour bar in the middle indicates the strain from -0.1 (compressive) to 0.1 (tensile). (**e**) Map of in-plane lattice parameter determined from the GPA map in **c**. The colour bar in the left indicates the change in lattice parameter from 3.7 to 3.9 Å. (**f**) Perspective view of the spatial distribution of T_c calculated from the local strain (Supplementary Fig. 3). The red and blue circles show the same area. Scale bar, 5 nm (**a,c–f**).

profiles from the central spot (000) to the reflection spots is then obtained for the measurement and the comparison of the positions of the reflection spots, as shown in Fig. 3b. The position of the 002 spot from circle I (green line) just slightly shift to the left in comparison with that from the circle II (black line), indicative of almost same c-lattice parameter in the irradiated FST film. On the other hand, the position of the 100 peak from local area I and II are not the same, indicative of large lattice variation along a axis parameter. We can calculate the strain map by geometrical phase analysis[53–55]. Figure 3c,d show the in-plane ε_{xx} (a axis direction) and the out-of-plane ε_{zz} (c axis direction) maps retrieved from the square area marked by the dash line in Fig. 3a. The averaged a- and c-lattice parameters were determined to be 3.77 and 5.95 Å, respectively, from the diffractogram of the whole image. The map of ε_{xx} (Fig. 3c) shows extreme spatial variation of strains. Deep valleys (blue) are the highly compressed region with compressive strain $\varepsilon_{xx} \cong -0.1$, whereas sharp peaks (yellow) are the highly stretched region with tensile strain $\varepsilon_{xx} \cong 0.1$. These two extreme domains are nanoscopically entangled with each other in the irradiated FST film. This is in striking contrast to the map of ε_{zz} in Fig. 3d, which is dominated by large interconnected areas of weak, strained areas. In contrast to the large strain observed in the irradiated FST film, the unirradiated FST film shows little strain in both in-plane ε_{xx} and out-of-plane ε_{zz} (Supplementary Fig. 2). From the ε_{xx} in the irradiated FST film, we can calculate lattice parameter map: $a = a_0(1 + \varepsilon_{xx})$, where a_0 is the lattice parameter from the reference area (solid blue circle in Fig. 3a). The result is

shown in Fig. 3e. We noticed that low-energy proton irradiation causes more than 5% variation in lattice parameter a ranging from 3.7 to 3.9 Å over merely a few nanometre scale randomly distributed in the FST films. Red circles in Fig. 3a–f show the same area containing one cascade defect. Under electron, neutron or ion irradiation, point defect clusters are also produced in the form of vacancy and interstitial clusters from collision cascade defects in irradiated materials[20,21,51,52]. These clusters could cause the great compression-–tension strain fields at a nanoscale alongside the cascade defects.

It is well known that compressive strain, especially along the in-plane direction, plays a crucial role in enhancing T_c in FST films[16,41–43]. Now, we attempt to correlate the strain and T_c in the irradiated films quantitatively, based on the analysis given by Bellingeri *et al.*[41], that a axis lattice parameter is approximately linearly proportional to T_c. A three-dimensional false-colour image in Fig. 3f shows the spatial variation of T_c obtained by using the linear relation given by Bellingeri *et al.*[41] (Supplementary Fig. 3). High-T_c (highly compressive) and low-T_c (highly tensile) regions are linked in a network similar to a cobweb in the irradiated FST films, with the highest T_c reaching ~ 25 K and the lowest T_c reaching ~ 15 K. The enhanced T_c regions in the irradiated FST film rises from these contracted lattice parameter domains (highly compressive strain region) that are just 5 nm apart in average. This distance is comparable to the superconducting coherence length of $FeSe_{1-x}Te_x(0.5 < x < 0.85)$, estimated to be around 2.6 nm at zero temperature using the
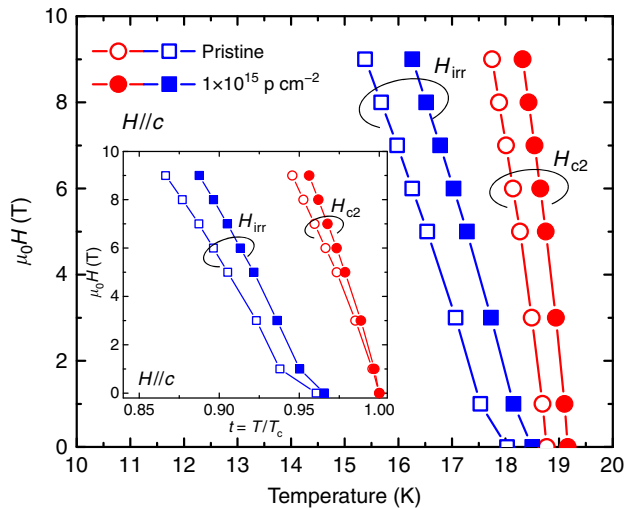
Figure 4 | Upper critical field and irreversibility field. Upper critical field $H_{c2}(T)$ and irreversible field $H_{irr}(T)$ ($H//c$) as a function of temperature up to 9 T//c for FST films before and after proton irradiation determined from Fig. 1. Inset: normalized temperature ($t = T/T_c$) dependence of H_{c2} and H_{irr} for the same field orientation. Error bars are of a size smaller than the data points.

Ginzburg–Landau theory[56,57]. The irradiated FST films consist of small puddles of different T_c values as shown in Fig. 3f. Proximity effect should lead to near homogeneous T_c ($T_c^{zero} \sim 18$ K) in the film as a whole. There is greater volume associated with the compressive strain in a axis direction than that with tensile strain in the irradiated FST films, resulting in the higher value of T_c as demonstrated in Fig. 1.

Irreversibility field and upper critical field. Now, we turn our attention to vortex pinning behaviour in the irradiated FST films. Figure 4 shows the temperature dependence of irreversibility field H_{irr} and H_{c2} for $H//c$. Both H_{irr} and H_{c2} shift to higher T for the proton-irradiated film. When plotted as a function of $t = T/T_c$, H_{irr} and H_{c2} increase after proton irradiation can be compared. We found the increase in H_{irr} is even more significant and produces a larger pinned vortex region, which suggests the cascade defects are strong pinning centres[20,21,58]. This is particularly important for the potential applications of the iron-based superconductor, as it can be operated in a larger-phase space.

J_c in high magnetic field up to 34.5 T. Strong enhancement of J_c is shown in Fig. 5a, where we plot $J_c(H)$ for $H//c$ at 4.2 K for 190 keV proton irradiation. The irradiated FST film has a larger self- and in-field J_c than the pristine film. The self-field J_c enhances from 0.9 MA cm^{-2} up to 1.4 MA cm^{-2}. Normalized $J_c(H)$ dependence of the FST films before and after irradiation is shown in a log–log pot in Fig. 5b. The regime of a nearly constant J_c up to a characteristic crossover field of B^* (90% of normalized $J_c(H)$), is associated with a single vortex pinning regime, followed by a rollover to a power-law regime ($J_c \propto B^{-\alpha}$) at intermediate fields, at which vortex–vortex interactions become relevant and a collective pinning vortex motion is dominant. We found that the pristine FST film already has high B^* of 0.26 T, which is higher than BaFe$_2$As$_2$:P + BaZrO$_3$ films[8]. After proton irradiation, B^* in the FST film increases up to 0.40 T. Studies by Dam et al.[59] showed that no correlation is found between the density of linear defects and the value of J_c in the single vortex-pinning regime. The ratio between B^*'s before and after irradiation is almost the same as the one between self-field J_c's. Thus, the increase in B^* after irradiation might just come from the increase in the self-
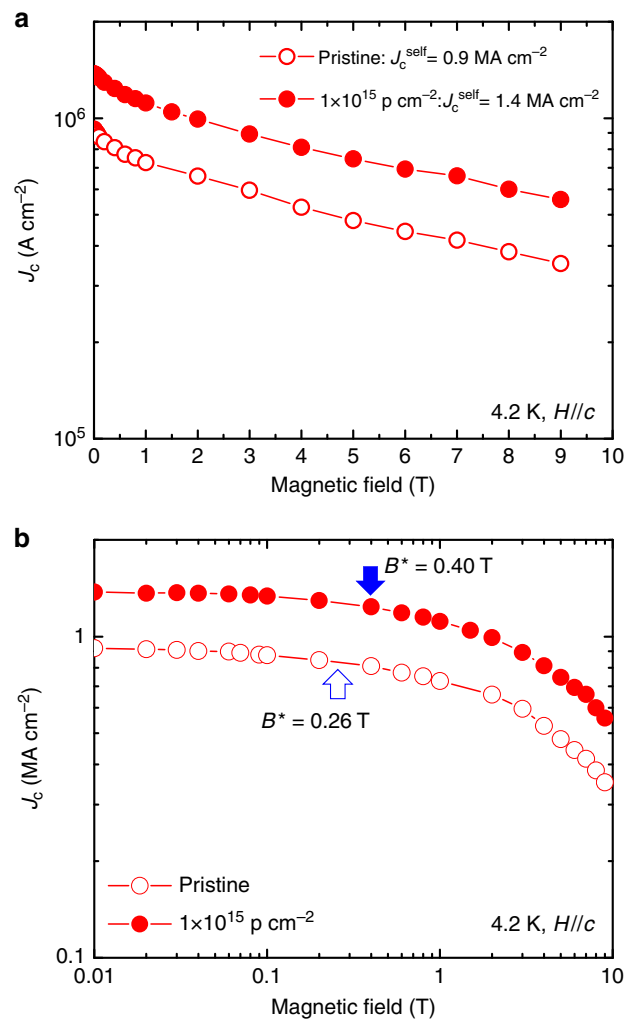

Figure 5 | Critical current density as a function of magnetic fields up to 9 T. (**a**) $J_c(H//c)$ for the FST film before and after 190 keV proton irradiation with 1×10^{15} p cm^{-2} dose at 4.2 K. (**b**) Same data plotted in log-log scale. The arrows indicate the field of the crossover field B^*.

field J_c. At intermediate field, however, $J_c(H)$ in both FST films does not follow a power-law decay, although we observe a roundish J_c dependence with magnetic field, as shown in Fig. 5b. The similar behaviour, that is, the absence of a power-law decay (or almost no change in α), has been found in both cuprate and iron-based superconducting films with strong vortex pinning[6–8,60]. It appears the irradiated FST films also exhibit an extremely good J_c retention at low field, indicating the potential of the iron-based superconductors for utility cable application.

High-magnetic field transport measurement of the irradiated FST film was performed up to 34.5 T. Figure 6a,b show $J_c(H)$ at various temperatures for $H//c$ and $H//ab$, respectively. In Fig. 6c,d, we plot $J_c(H)$ for the irradiated FST film at 4.2 and 12 K, together with the $J_c(H)$ data taken on the pristine film[16] for comparison. The irradiated FST film clearly has a much better field performance for both $H//ab$ and $H//c$. We found the J_c at 12 K increased by one order of magnitude after irradiation over 15 T for $H//ab$ and over 6 T for $H//c$. Enhancement of vortex pinning at higher temperature (12 K) is much more significant compared with that at low temperature (4.2 K).

Vortex-pinning properties. The effect of cascade defects and strain modulation from proton irradiation on vortex pinning
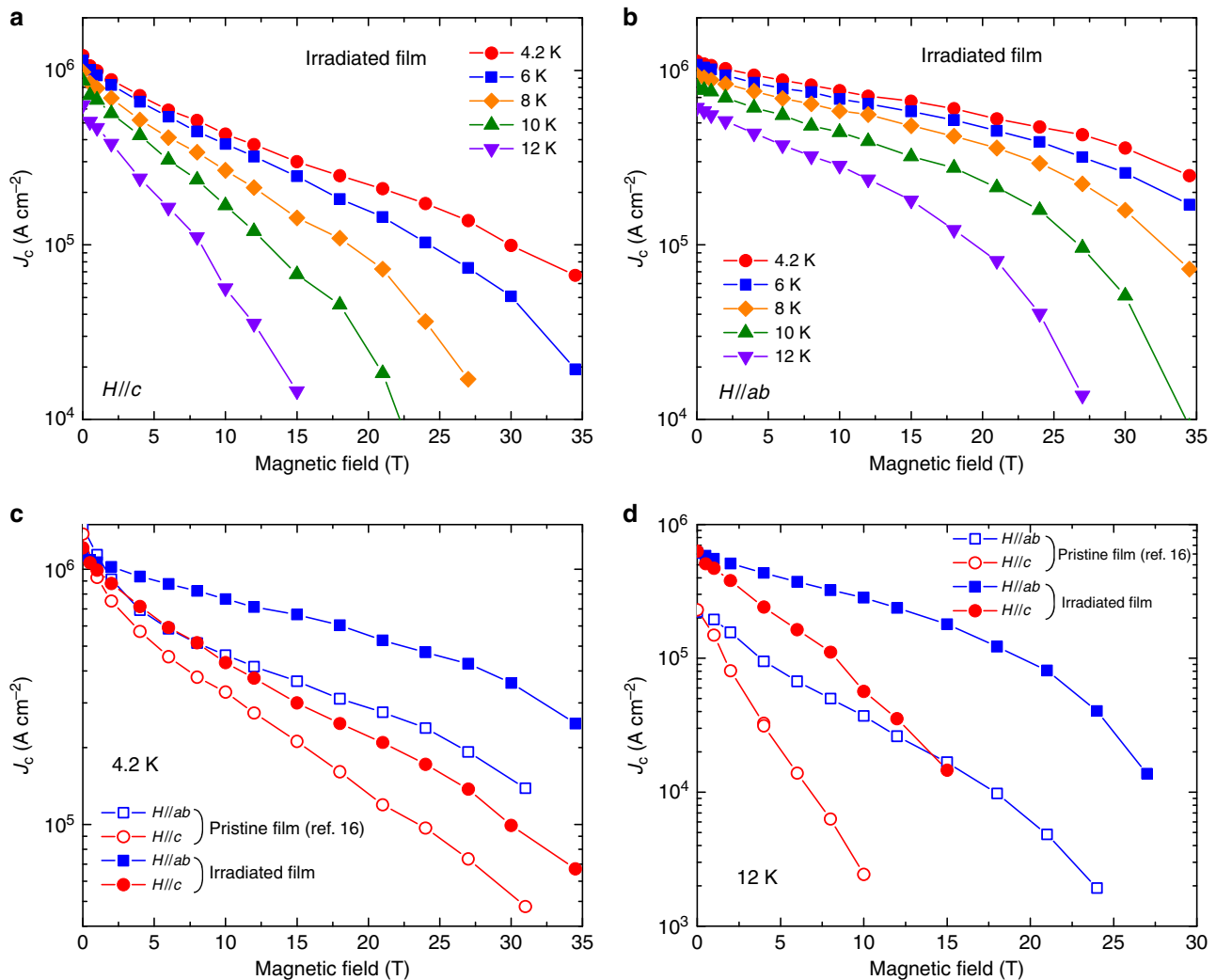
Figure 6 | High-field critical current density up to 34.5 T. (**a,b**) $J_c(H)$ for proton-irradiated FST film with 1×10^{15} p cm^{-2} dose at different temperature up to 34.5 T with $H//c$ and $H//ab$, respectively. (**c,d**) $J_c(H)$ for the irradiated FST film up to 34.5 T compared with the pristine FST film[16] at 4.2 and 12 K, respectively.

properties can be appreciated by evaluating the pinning force $F_p = J_c \times \mu_0 H$. Figure 7a shows $F_p(H)$ for the pristine[16] and the irradiated FST films at 4.2 K together with the data for NbTi (ref. 61) and Nb$_3$Sn (ref. 62) wires for comparison. After proton irradiation, the F_p peak width broadens and the enhancement of F_p is prominent in the high-field region for $H//c$. The maximum pinning force $F_{p,max} \sim 45$ GN m^{-3}, which is increased by $\sim 30\%$, occurs at 12 T in the irradiated FST film for $H//c$. At $H//ab$, a remarkably high $F_{p,max}$ of ~ 120 GN m^{-3} is reached for the irradiated FST film at 27 T, that is, an enhancement of $\sim 200\%$ over the pristine film. These results suggest that the cascade defects and nanoscale strain field can be highly effective pinning centres, especially for $H//ab$. Extensive researches by Llordés et al.[63] and Deutscher[64] have showed a similar result that the nanoscale strain present in ε_{zz} map is responsible for a strong enhancement of pinning force for $H//c$. In the irradiated FST film, the nanoscale strain observed in ε_{xx} map can lead to the extremely high $F_{p,max}$ and the shift of the $F_{p,max}$ to high field for $H//ab$.

The reduced pinning force density $f_p = F_p/F_{p,max}$ as a function of reduced magnetic field $h = H/H_{irr}$ for the pristine[16] and the irradiated FST films at 12 K is plotted in Fig. 7b,c, respectively. Solid and dashed fitting lines are calculated using $f_p = f_{p0} h^p (1-h)^q$, where f_{p0} is a constant. The values of exponent fitting parameters p and q are given in the

Supplementary Table 1. After irradiation, we found that the exponent p increases significantly to 0.57 for $H//c$ from 0.33 before the irradiation, whereas for $H//ab$, p increases to 0.97 (towards unity) from 0.85 before the irradiation. The exponent q decreases substantially to 1.87 ($H//c$) and 1.56 ($H//ab$) from the values of 2.63 ($H//c$) and 2.68 ($H//ab$) before the irradiation. It is perhaps instructive to compare our results with the vortex pinning for α-Ti ribbon in Nb-Ti wires, which shows that cold work reduces the dimensions of the α-Ti precipitates to optimum size for vortex pinning, resulting in the F_p curve shape $F_p \sim h(1-h)$ (refs 65,66). Of course, rigorous analysis and modelling would need to take into account of accurate information on the defect size, associated strain field and morphology/anisotropy, which is beyond the current studies. Nevertheless, both fitting parameters p and q are found approaching unity in the irradiated films, which is consistent with the structural observation shown in Fig. 3. The cascade defect and nanoscale strain act more or less similar to elongated point-defect pinning. The scaling behaviour $F_p = h^{0.97}(1-h)^{1.56}$ for $H//ab$ of the irradiated FST film may be attributed to strong vortex pinning due to a dense array of nanoscale cascade defect and longer extension of the strain field along the a axis direction.

In conclusion, a robust enhancement of T_c and J_c has been realized simultaneously in the FST film irradiated with
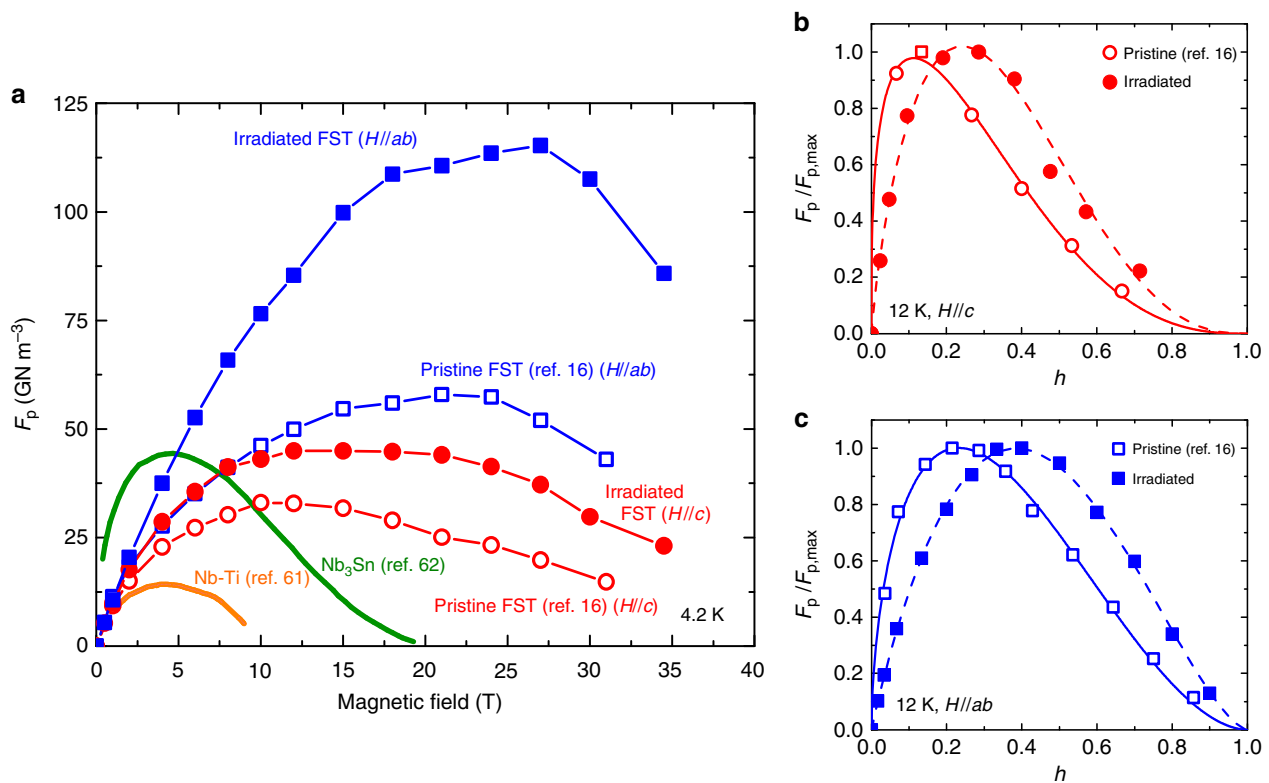
Figure 7 | High-field pinning force. (**a**) $F_p(H)$ for FST film before and after 190 keV proton irradiation with 1×10^{15} p cm^{-2} dose at 4.2 K, compared with NbTi (ref. 61) and Nb$_3$Sn (ref. 62) wires. (**b**,**c**) Normalized $F_p(h)$ for FST film before (open symbols) and after (close symbols) proton irradiation at 12 K for $H//c$ and $H//ab$, respectively, whereas solid (before) and dashed (after) lines are the corresponding fitting curves.

1×10^{15} p cm^{-2} dose of 190 keV proton, resulting in an increase of T_c^{zero} from 18.0 to 18.5 K and a self-field J_c enhancement from 0.9 MA cm^{-2} up to 1.4 MA cm^{-2} at 4.2 K. TEM structural characterization provides direct atomic-scale imaging of the collision cascade defects and the surrounding strain field, produced by low-energy proton irradiation. The highly compressive strain increases T_c of the irradiated films through the proximity effect. The cascade defects and nanoscale strain are found to provide strong vortex pinning, leading to the increase of J_c by one order of magnitude at 12 K over 6 T and record high $F_{p,max}$ of ~ 120 GN m^{-3} for $H//ab$ at 27 T and 4.2 K. This study demonstrates that it is possible to achieve significant enhancement of J_c without T_c reduction through the design of vortex pinning landscape that takes advantage of cascade defects and associated strain field. Further improvement of the performance of these films can be expected with fine tuning of the morphology of defects and strain configuration. The low-energy ion sources are inexpensive to operate and are readily available commercially. This route provides a practical solution to the central limiting factor that controls the performance of superconducting wires and tapes that underpins all superconducting applications.

Methods

Sample preparation. FST films of 100–130 nm thickness are grown by pulsed laser deposition with CeO$_2$ buffer layer on SrTiO$_3$ single-crystalline substrates[15,16,46]. The FST films characterized in advance were covered by 1.5 μm thick Al foil and irradiated with 190 keV protons at dose of 1×10^{15} p cm^{-2} (Supplementary Fig. 1). At this energy, the simulation using the stopping range of ions in matter code[47] shows that the stopping region (Bragg peak) of the protons is ~ 100 nm from the FST film surface, which maximizes the effect of cascade defect creations in the FST films.

Characterization. Microstructures of the 190 keV proton-irradiated FST film were characterized using aberration-corrected STEM and HRTEM.

All transport characterizations were performed on the same films before and after irradiation. Low-field measurements were performed by the standard four-probe method in a physical property measurement system (Quantum Design), whereas the high-field measurements were done in 35 T direct current magnet at National High Magnetic Field Laboratory in Tallahassee.

Data availability. All relevant data supporting the finding of this study are available within the article and its Supplementary Information file or available from the corresponding authors upon request, which should be addressed to T.O. and Q.L.

References

1. Larbalestier, D., Gurevich, A., Feldmann, D. M. & Polyanskii, A. High-T_c superconducting materials for electric power applications. *Nature* **414,** 368–377 (2001).

2. Larbalestier, D. *et al.* Isotropic round-wire multifilament cuprate superconductor for generation of magnetic fields above 30 T. *Nat. Mater.* **13,** 375–381 (2014).

3. Civale, L. *et al.* Vortex confinement by columnar defects in YBa$_2$Cu$_3$O$_7$ crystals: Enhanced pinning at high fields and temperatures. *Phys. Rev. Lett.* **67,** 648–651 (1991).

4. Haugan, T., Barnes, P. N., Wheeler, R., Meisenkothen, F. & Sumption, M. Addition of nanoparticle dispersions to enhance flux pinning of the YBa$_2$Cu$_3$O$_{7-x}$ superconductor. *Nature* **430,** 867–870 (2004).

5. MacManus-Driscoll, J. L. *et al.* Strongly enhanced current densities in superconducting coated conductors of YBa$_2$Cu$_3$O$_{7-x}$ + BaZrO$_3$. *Nat. Mater.* **3,** 439–443 (2004).

6. Gutiérrez, J. *et al.* Strong isotropic flux pinning in YBa$_2$Cu$_3$O$_{7-x}$ − BaZrO$_3$ films derived from chemical solutions. *Nat. Mater.* **6,** 367–373 (2007).

7. Maiorov, B. *et al.* Synergetic combination of different types of defect to optimize pinning landscape using BaZrO$_3$-doped YBa$_2$Cu$_3$O$_7$. *Nat. Mater.* **8,** 398–404 (2009).

8. Miura, M. *et al.* Strongly enhanced flux pinning in one-step deposition of BaFe$_2$(As$_{0.66}$P$_{0.33}$)$_2$ superconductor films with uniformly dispersed BaZrO$_3$ nanoparticles. *Nat. Commun.* **4,** 2944 (2013).

9. Lee, S. *et al.* Artificially engineered superlattices of pnictide superconductors. *Nat. Mater.* **12**, 392–396 (2013).

10. Sato, H., Hiramatsu, H., Kamiya, T. & Hosono, H. High critical-current density with less anisotropy in BaFe$_2$(As,P)$_2$ epitaxial thin films: effect of intentionally grown c-axis vortex-pinning centers. *Appl. Phys. Lett.* **104**, 182603 (2014).

11. Kamihara, Y., Watanabe, T., Hirano, M. & Hosono, H. Iron-based layered superconductor La[O$_{1−x}$F$_x$]FeAs ($x = 0.05 − 0.12$) with $T_c = 26$ K. *J. Am. Chem. Soc.* **130**, 3296–3297 (2008).

12. Putti, M. *et al.* New Fe-based superconductors: properties relevant for applications. *Supercond. Sci. Technol.* **23**, 034003 (2010).

13. Gurevich, A. Iron-based superconductors at high magnetic fields. *Rep. Prog. Phys.* **74**, 124501 (2011).

14. Tarantini, C. *et al.* Development of very high J_c in Ba(Fe$_{1−x}$Co$_x$)$_2$As$_2$ thin films grown on CaF$_2$. *Sci. Rep.* **4**, 7305 (2014).

15. Li, Q., Si, W. & Dimitrov, I. K. Films of iron chalcogenide superconductors. *Rep. Prog. Phys.* **74**, 124510 (2011).

16. Si, W. *et al.* High current superconductivity in FeSe$_{0.5}$Te$_{0.5}$-coated conductors at 30 tesla. *Nat. Commun.* **4**, 1347 (2013).

17. Iida, K. *et al.* Oxypnictide SmFeAs(O,F) superconductor: a candidate for high–field magnet applications. *Sci. Rep.* **3**, 2139 (2013).

18. Hänisch, J. *et al.* High field superconducting properties of Ba(Fe$_{1−x}$Co$_x$)$_2$As$_2$ thin films. *Sci. Rep.* **5**, 17363 (2015).

19. Roas, B. *et al.* Irradiation induced enhancement of the critical current density of epitaxial YBa$_2$Cu$_3$O$_{7−x}$ thin films. *Appl. Phys. Lett.* **54**, 1051–1053 (1989).

20. Kirk, M. A. Structure and flux pinning properties of irradiation defects in YBa$_2$Cu$_3$O$_{7−x}$. *Cryogenics* **33**, 235–242 (1993).

21. Kirk, M. A. & Yan, Y. Structure and properties of irradiation defects in YBa$_2$Cu$_3$O$_{7−x}$. *Micron* **30**, 507–526 (1999).

22. Huang, D. X. *et al.* Damage morphology along ion traces in Au-irradiated Bi$_2$Sr$_2$CaCu$_2$O$_x$. *Phys. Rev. B* **57**, 13907–13914 (1998).

23. Summers, G. P., Burke, E. A., Chrisey, D. B., Nastasi, M. & Tesmer, J. R. Effect of particle-induced displacements on the critical temperature of YBa$_2$Cu$_3$O$_{7−δ}$. *Appl. Phys. Lett.* **55**, 1469–1471 (1989).

24. Matsui, H. *et al.* 4-fold enhancement in the critical current density of YBa$_2$Cu$_3$O$_7$ films by practical ion irradiation. *Appl. Phys. Lett.* **101**, 232601 (2012).

25. Jia, Y. *et al.* Doubling the critical current density of high temperature superconducting coated conductors through proton irradiation. *Appl. Phys. Lett.* **103**, 122601 (2013).

26. Rupich, M. W. *et al.* Engineered pinning landscapes for enhanced 2G coil wire. *IEEE Trans. Appl. Supercond.* **26**, 6601904 (2016).

27. Tamegai, T. *et al.* Effects of particle irradiations on vortex states in iron-based superconductors. *Supercond. Sci. Technol.* **25**, 084008 (2012).

28. Fang, L. *et al.* High, magnetic field independent critical currents in (Ba,K)Fe$_2$As$_2$ crystals. *Appl. Phys. Lett.* **101**, 012601 (2012).

29. Fang, L. *et al.* Huge critical current density and tailored superconducting anisotropy in SmFeAsO$_{0.8}$F$_{0.15}$ by low-density columnar-defect incorporation. *Nat. Commun.* **4**, 2655 (2013).

30. Eisterer, M. *et al.* Anisotropic critical currents in FeSe$_{0.5}$Te$_{0.5}$ films and the influence of neutron irradiation. *Supercond. Sci. Technol.* **24**, 065016 (2011).

31. Maiorov, B. *et al.* Competition and cooperation of pinning by extrinsic point-like defects and intrinsic strong columnar defects in BaFe$_2$As$_2$ thin films. *Phys. Rev. B* **86**, 094513 (2012).

32. Yeh, K. -W. *et al.* Tellurium substitution effect on superconductivity of the α-phase iron selenide. *Europhys. Lett.* **84**, 37002 (2008).

33. Mizuguchi, Y., Tomioka, F., Tsuda, S., Yamaguchi, Y. & Takano, Y. Superconductivity at 27 K in tetragonal FeSe under high pressure. *Appl. Phys. Lett.* **93**, 152505 (2008).

34. Medvedev, S. *et al.* Electronic and magnetic phase diagram of β-Fe$_{1.01}$Se with superconductivity at 36.7 K. *Nat. Mater.* **8**, 630–633 (2009).

35. Mizuguchi, Y., Deguchi, K., Tsuda, S., Yamaguchi, T. & Takano, Y. Moisture-induced superconductivity in FeTe$_{0.8}$S$_{0.2}$. *Phys. Rev. B* **81**, 214510 (2010).

36. Kawasaki, Y. *et al.* Phase diagram and oxygen annealing effect of FeTe$_{1−x}$Se$_x$ iron-based superconductor. *Solid State Commun.* **152**, 1135–1138 (2012).

37. Sun, Y. *et al.* Dynamics and mechanism of oxygen annealing in Fe$_{1+y}$Te$_{0.6}$Se$_{0.4}$ single crystal. *Sci. Rep.* **4**, 4585 (2014).

38. Ozaki, T. *et al.* Fabrication of binary FeSe superconducting wires by diffusion process. *J. Appl. Phys.* **111**, 112620 (2012).

39. Wang, Q. Y. *et al.* Interface-induced high-temperature superconductivity in single unit-cell FeSe films on SrTiO$_3$. *Chin. Phys. Lett.* **29**, 037402 (2012).

40. Ge, J.-F. *et al.* Superconductivity above 100 K in single-layer FeSe films on doped SrTiO$_3$. *Nat. Mater.* **14**, 285–289 (2015).

41. Bellingeri, E. *et al.* Critical temperature enhancement by biaxial compressive strain in FeSe$_{0.5}$Te$_{0.5}$ thin films. *J. Supercond. Nov. Magn.* **24**, 35–41 (2011).

42. Ichinose, A. *et al.* Induced lattice strain in epitaxial Fe-based superconducting films on CaF$_2$ substrates: a comparative study of the microstructures of SmFeAs(O,F), Ba(Fe,Co)$_2$As$_2$, and FeTe$_{0.5}$Se$_{0.5}$. *Appl. Phys. Lett.* **104**, 122603 (2014).

43. Imai, Y., Sawada, Y., Nabeshima, F. & Maeda, A. Suppression of phase separation and giant enhancement of superconducting transition temperature in FeSe$_{1−x}$Te$_x$ thin films. *Proc. Natl Acad. Sci. USA* **112**, 35–41 (2015).

44. Jung, S.-G. *et al.* Enhanced critical current density in the pressure-induced magnetic state of the high-temperature superconductor FeSe. *Sci. Rep.* **5**, 16385 (2015).

45. Liu, T. J. *et al.* Charge-carrier localization induced by excess Fe in the superconductor Fe$_{1+y}$Te$_{1−x}$Se$_x$. *Phys. Rev. B* **80**, 174509 (2009).

46. Si, W. *et al.* Iron-chalcogenide FeSe$_{0.5}$Te$_{0.5}$ coated superconducting tapes for high field applications. *Appl. Phys. Lett.* **98**, 262509 (2011).

47. Ziegler, J. F., Biersack, J. P. & Littmark, U. *The Stopping and Range of Ions in Solids* (Pergamon, 1985).

48. Anderson, P. W. Theory of dirty superconductors. *J. Phys. Chem. Solids* **11**, 26–30 (1959).

49. Alloul, H. *et al.* Defects in correlated metals and superconductors. *Rev. Mod. Phys.* **81**, 45 (2009).

50. Paglione, J. & Greene, R. L. High-temperature superconductivity in iron-based materials. *Nat. Phys.* **6**, 645–658 (2010).

51. Frischherz, M. C., Kirk, M. A., Zhang, J. P. & Weber, H. W. Transmission electron microscopy of defect cascades in YBa$_2$Cu$_3$O$_{7−δ}$ produced by ion irradiation. *Phil. Mag. A* **67**, 1347–1363 (1993).

52. Frischherz, M. C., Kirk, M. A., Farmer, J., Greenwood, L. R. & Weber, H. W. Defect cascades produced by neutron irradiation in YBa$_2$Cu$_3$O$_{7−δ}$. *Phys. C* **232**, 309–327 (1994).

53. Hÿtch, M. J., Putaux, J.-L. & Pénisson, J.-M. Measurement of the displacement field of dislocations to 0.03 Å by electron microscopy. *Nature* **423**, 270–273 (2003).

54. Hÿtch, M. J., Snoeck, E. & Kilaas, R. Quantitative measurement of displacement and strain fields from HREM micrographs. *Ultramicroscopy* **74**, 131–146 (1998).

55. Wu, L. *et al.* Nanostructures and defects in thermoelectric AgPb$_{18}$SbTe$_{20}$ single crystal. *J. Appl. Phys.* **105**, 094317 (2009).

56. Fang, M. *et al.* Weak anisotropy of the superconducting upper critical field in Fe$_{1.11}$Te$_{0.6}$Se$_{0.4}$ single crystals. *Phys. Rev. B* **81**, 020509 (R) (2010).

57. Khim, S. *et al.* Evidence for dominant Pauli paramagnetic effect in the upper critical field of single-crystalline FeTe$_{0.6}$Se$_{0.4}$. *Phys. Rev. B* **81**, 184511 (2010).

58. Brown, B. S., Blewitt, T. H., Wozniak, D. G. & Suenaga, M. Critical current changes in Nb$_3$Sn irradiated with fast neutrons at 6 K. *J. Appl. Phys.* **46**, 5163–5168 (1975).

59. Dam, B. *et al.* Origin of high critical currents in YBa$_2$Cu$_3$O$_{y−δ}$ superconducting films. *Nature* **399**, 439–442 (1999).

60. Solovyov, V., Dimitrov, I. K. & Li, Q. Growth of thick YBa$_2$Cu$_3$O$_7$ layers via a barium fluoride process. *Supercond. Sci. Technol.* **26**, 013001 (2013).

61. Cooley, L. D., Lee, P. J. & Larbalestier, D. C. Flux-pinning mechanism of proximity-coupled planar defects in conventional superconductors: evidence that magnetic pinning is the dominant pinning mechanism in niobiumtitanium alloy. *Phys. Rev. B* **53**, 6638–6652 (1996).

62. Godeke, A. A review of the properties of Nb$_3$Sn and their variation with A15 composition, morphology and strain state. *Supercond. Sci. Technol.* **19**, R68 (2006).

63. Llordés, A. *et al.* Nanoscale strain-induced pair suppression as a vortex-pinning mechanism in high-temperature superconductors. *Nat. Mater.* **11**, 329–336 (2012).

64. Deutscher, G. The role of Cu-O bond length fluctuations in the high temperature superconductivity mechanism. *J. Appl. Phys.* **111**, 112603 (2012).

65. Meingast, C. & Larbalestier, D. C. Quantitative description of a very high critical current density Nb-Ti superconductor during its final optimization strain. II. Flux pinning mechanisms. *J. Appl. Phys.* **66**, 5971–5983 (1989).

66. Meingast, C., Lee, P. J. & Larbalestier, D. C. Quantitative description of a high J_c Nb-Ti superconductor during its final optimization strain. II. Microstructure, T_c, H_{c2}, and resistivity. *J. Appl. Phys.* **66**, 5962–5970 (1989).

Acknowledgements

Author contributions

T.O. and Q.L. designed the study, and with L.W. wrote the manuscript. W.S., T.O. and C.Z. made the thin films. T.O. and Q.L. did the low-field (≤ 9 T) superconducting property measurement. T.O., C.Z. and J.J. carried out the high-field measurement. L.W., J.Z. and Y.Z. performed TEM studies. Q.L., T.O. and L.W. analysed the data. Q.L. directed the project. All the authors contributed to discussion on the results for the manuscript.

Additional information